Radiation Physics and Chemistry 167 (2020) 108244

Contents lists available at ScienceDirect

Radiation Physics and Chemistry

journal homepage: www.elsevier.com/locate/radphyschem

Multi-spectral X-ray transmission imaging using a BSI CMOS Image Sensor

José Lipovetzky[a,b,c,d,*], Andrés Cicuttin[d], María Liz Crespo[d], Miguel Sofo Haro[a,c], Fabricio Alcalde Bessia[b,c], Martín Pérez[a,c], Mariano Gómez Berisso[b,c]

[a] Comisión Nacional de Energía Atómica (CNEA), Centro Atómico Bariloche (CAB), Argentina
[b] Consejo Nacional de Investigaciones Científicas y Técnicas (CONICET), Argentina
[c] Instituto Balseiro, Universidad Nacional de Cuyo, Argentina
[d] The Abdus Salam International Centre for Theoretical Physics (ICTP), Italy

ARTICLE INFO

Keywords:
CMOS image detectors
Ionizing radiation
X-rays
Imaging

ABSTRACT

In this work we study the performance to obtain X-ray images of a Back Side Illuminated CMOS Image Sensor, the Omnivision OV5647, empoying X-rays from tube with a palladium anode and voltages from 7.5 keV to 50 keV. The performance is compared with the Timepix detector operating in the Time Over Threshold mode. False color images are obtained using data from different energies and brightnesses, to fussion different information on the same picture. The different attenuations are analyzed and discussed in terms of the charge detection efficiency of the CMOS sensor, measured using Fluorescence X-rays and gamma rays from calibrated sources.

1. Introduction

CMOS Image Sensors (CIS), originally designed for visible light imaging in consumer electronics, have been also used for gamma rays dosimetry (Conti et al., 2013; Paolucci et al., 2011); detection and classification of alpha particles in mixed beams (Perez et al., 2016); for the detection of thermal neutrons using conversion layers (Pérez et al., 2018); for x-Ray spectrography (Zhao and Sakurai, 2017) and the obtention of spectral fluorescence images [25]; and to acquire high resolution X-ray images (Alcalde Bessia et al., 2018). Back Side Illuminated (BSI) CIS are specially thinned chips in which the incoming light impringes the sensitive area without trespassing the metal and gate layers of the chip, allowing a higher pixel fill factor (Zhang et al., 2009). This is specially important to allow the fabrication of small pixels.

Compared to other hybrid pixels detectors specially designed for ionizing radiation detection (Ballabriga et al., 2016), BSI CIS have a smaller pixel pitch, allowing higher spatial resolution (Alcalde Bessia et al., 2018). On the other hand, most hibrid pixel detectors allow the acquisition of spectroscopic X-ray images, separating the contribution from different photon energies. This allows better image qualities using the same dose, and allows material composition analysis taking advantage of the spectral dependence of X-ray absorption in different materials (Ballabriga et al., 2016; Procz et al., 2010; Jakuubek, 2009). The strong photon energy dependence close to the k-edge of a material, allows the identification of a specific contrast material for example in digital radiography (Schlomka et al., 2008) or computed tomography (Schlomka et al., 2008). The energy separation is usually implemented through the use of multiple thresholds in photon counting imaging systems (Ballabriga et al., 2016). In X-ray inspection of baggage in airport security systems multiple X-ray energies are used, and image processing techniques fussion spectral data in a single picture with relevant information for the operator (Dmitruk et al., 2017).

This paper deals with the possibility of using a BSI CIS to obtain high spatial resolution X-ray transmission images with different information obtained with different photon energies. One posible way to do this would be to take advantage of the ability of the BSI CIS to determine the photon energy, as is done by (Zhao and Sakurai, 2017, 2019). In those works, the authors show the ability to obtain fluorescence spectrums up to 9.6 keV measuring the charge deposited by each event. However, the spectroscopy of photons of larger energies is more difficult because of the limmited Full Well Capacity of these sensors which limits the maximum photon energy to values lower than the maximum energy used in this work to penetrate e.g. metal layers of hundreds of micrometers. Thus, the approach of the present work is to obtain a colection of images with different photon spectra, increasing the X-ray tube voltage, and using the BSI CIS to integrate the whole charge deposited by the photons. Using a packaged integrated circuit as a case study, we present the images obtained with different X-ray tube voltages, discuss the different information which can be determined, and present as an example the fussion of the whole information in a

* Corresponding author. Comisión Nacional de Energía Atómica (CNEA), Centro Atómico Bariloche (CAB), Argentina.
E-mail address: lipo@ib.edu.ar (J. Lipovetzky).

https://doi.org/10.1016/j.radphyschem.2019.03.048
Received 15 December 2018; Received in revised form 28 March 2019; Accepted 31 March 2019
Available online 04 April 2019
0969-806X/

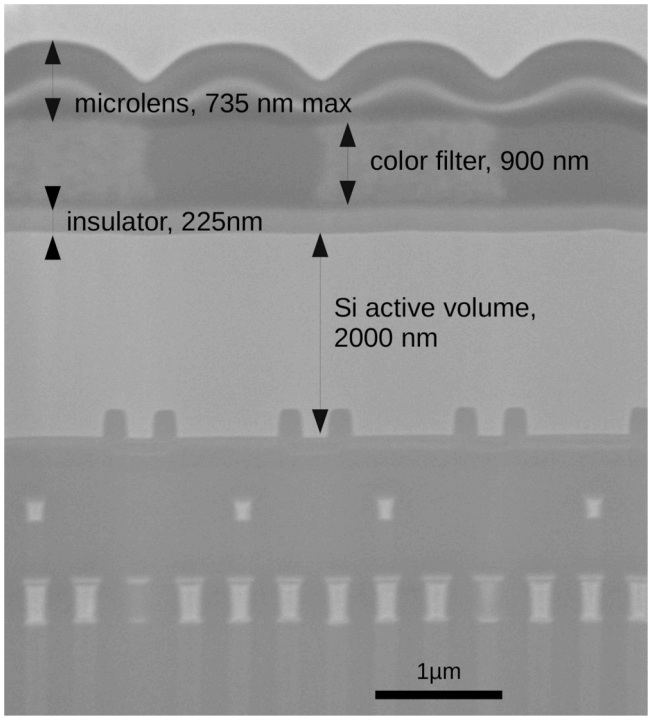

Fig. 1. SEM cross section of four BSI CIS pixels. After (Alcalde Bessia et al., 2018).

single false color picture. With this approach, not only high resolution X-ray images can be obtained, it is also possible to estimate aditional information from the multiespectral images e.g. material composition, in a method complementary to the fluorescence reported by [25] and (Zhao and Sakurai, 2017).

The next section describes the devices used in this work. Section 3 presents the performance of the BSI CSI as an X-ray imager and comparing it to the Timepix2 detector. Section 5 discusses the results obtaining transmission X-ray images. Then, in section 4 we present the detection efficiency of the sensor. Finally section 5 compares the performance of both sensors and section 6 presents the conclusions.

2. Detectors

The BSI CIS used in this work is the OmniVision OV5647 1/4" chip. It has a 2592 × 1944 pixels, with a pixel pitch of 1.4 × 1.4 μm^2 and a 3.67 × 2.73 mm^2 active area. The BSI sensor has a sensitive Si detection volume with a thickness of 2.0 μm, covered by a thin insultator, a color filter to allow RGB images, and an array of microlens, as is shown in Fig. 1. The data from the sensor were acquired using a Raspberry Pi computer (Raspberry Pi development group, 2018) taking consecutive images, each image using an integration time of 5 s. Analog and digital gains were programed to 512 and 256 respectively. Under this configuration, at room temperature, the dark signal is much lower than the charge deposited by the X-ray photons used in this work. During all the measurements, the sensor was placed inside a plastic box with an open window in front of the active area, and covered with a 255 μm Al layer to block visible light.

Images obtained with the CIS are compared to images of the same object empoying a Imatek XRI-UNO camera (Jambi et al., 2015; Imatek, 2012), based on the Timepix detector. The Timepix sensor, developed by the Medipix collaboration, is a readout chip connected to a Si, Ge or CdTe sensitive volume (Llopart et al., 2007). The XRI-UNO camera used in this work comprises a 300 μm thick Silicon active detection volume. The sensor has 64 K pixels, with a pixel pitch of 55 × 55 μm^2 and a 14 × 14 mm^2 area, and through a proper threshold optimization has been used for spectroscopic X-ray imaging of an encapsulated circuit (Procz et al., 2009). The XRI-UNO camera shields the sensor from visible light with a thin carbon fiber layer.

3. X-ray transmission images

In this section we present the ability of a BSI CIS to acquire X-ray images with different X-ray spectra and compared to the Timepix detector. The sample to study was an integrated circuit—a quadruple NAND gate part number SN74HC03—, SOIC14 plastic package, similarly to what was used as a case study by (Procz et al., 2009).

It has been reported that CIS can be used with some limitations to quantify the energy of incoming photons up to energies of few keV (Holden et al., 2017, 2018). However, the full well capacity of the sensor of ≈ 4.3 ke^- (RaspberryFoundation. Came) poses a limit to the maximum energy which can be resolved with the sensor used in this work, taking in account that the mean energy to create an electron-hole pair is 3.6 eV. For that reason, our strategy to obtain images with spectral information was to use the sensor in integration mode—i.e. integrate the whole charge generated by the incoming photons—, taking several X-ray images using different X-ray spectra.

The different X-ray spectra were provided with the X-ray operated at different tube bias voltages (TBV). The X-ray source was an OXFORD Jupiter 5000 Series X-ray shielded tube, which can be powered with up to 50 kV, and has a spot size of 50 μm, with a palladium target. The TV was modified from 7.5 kV in steps of 2.5 keV or 5 keV up to 50 kV. The increase in TBV modifies the Bremsstrahlung emmision of the in two ways; in first place the total number of photons of any energy increases; and in second place, and since the high-end energy of the emmited spectrum is determined by the TBV, higher energy photons are emmited. With this TBV control, we were able to obtain X-ray images with different spectra without having photon energy classification in the detector.

3.1. Images varying TBV

X-ray images were obtained using the OV5674 BSI CIS and the state-of-the art Timepix detector. The CIS detector was placed at a distance of 30 cm from the source, and the sample to be radiographed was placed at 5 mm from the detector. Fig. 2 shows the images obtained at different TBV. The images show different information due to variations of the contrasts in various parts of the sample with built with different materials. For example, the low penetration of low energy X-rays causes a very high contrast along the whole package of the chip. As the TBV is increased, more energetic and penetrating photons provide a higher contrast, which allow the observation of the bonding fingers and pin extensions inside the plastic package. At high TBV where the population of high energy penetrating photons increases, the bonding wires can be observed between the central pad and the fingers.

The same object was radiographed using the Timepix sensor, operated in the MediPix mode, THR = 374, TBK = 132 after equalization and damaged pixel suppression. The sample was placed in contact of the window of the XRI-UNO camera, and the X-ray source placed at a distance of 50 cm from the detector, obtaining at different TBV values the images of Fig. 3.

Since the active area of the TimpePix is larger than the area of the CIS, the observed region of the sample is larger, but contains the same parts of interest, i.e. package, few pads and pins, and the pad with the Silicon IC.

3.2. Contrasts varying TBV

The use of several X-ray energies can provide extra information about the presence of different materials in the sample. Fig. 4 shows the X-ray transmission as a function of TBV for two different regions of the chip, the opaque bond fingers and more transparent plastic package,

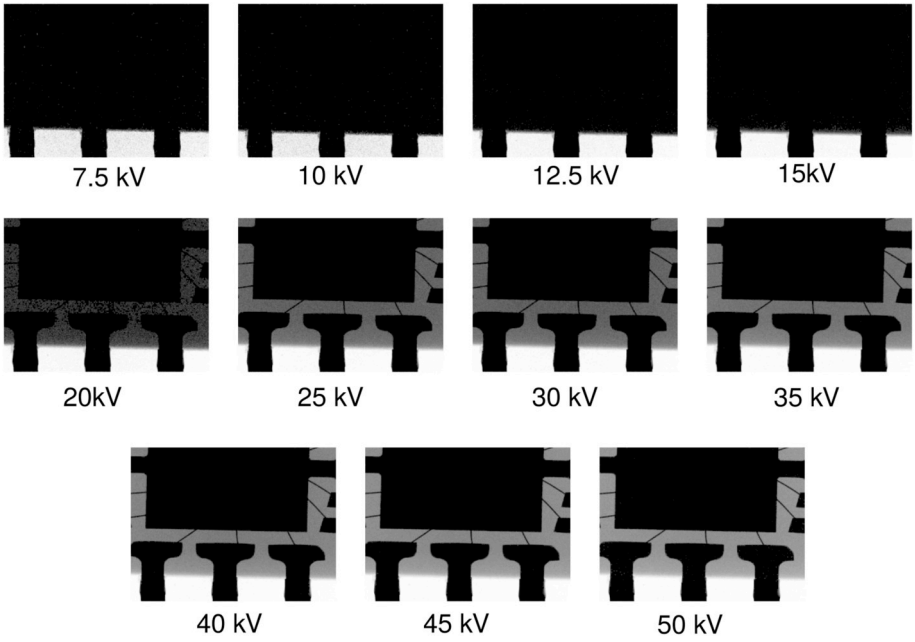

Fig. 2. Radiographic images at different using different X-ray tube voltages using the OV5647 BSI CIS detector. The Grayscale is normalized to have the same average brightness outside the chip.

obtained with the Timepix. As the TBV increases, the transmissions of the two regions increase due to the deeper penetration of the more energetic X-rays produced by the source. However, these transmissions has a different dependence in both regions of the sample. Fig. 5 presents the ratio between the attenuations of the two regions measured by the CIS and Timepix detectors as a function of TBV. The ratios between contrasts in the plastic package and the metal bonding fingers raises from 4 × at 10 kV to 57 × at 50 kV with the CIS; and from 1.8 times at 7.5 kV to 9.4 at 50 kV with the Timepix. This different ratio of contrasts at differnt TBV implies having different material compositions in the two regions of the sample. The differences between the CIS and Medipix will be discussed below.

On the other hand, the ratio of constrasts between the regions does not change so fast when the tube voltage incresases from 25 kV to 50 kV. However, the X-ray intensity of the beam incresases significantly and the penetration also increases by a factor of two. This implies

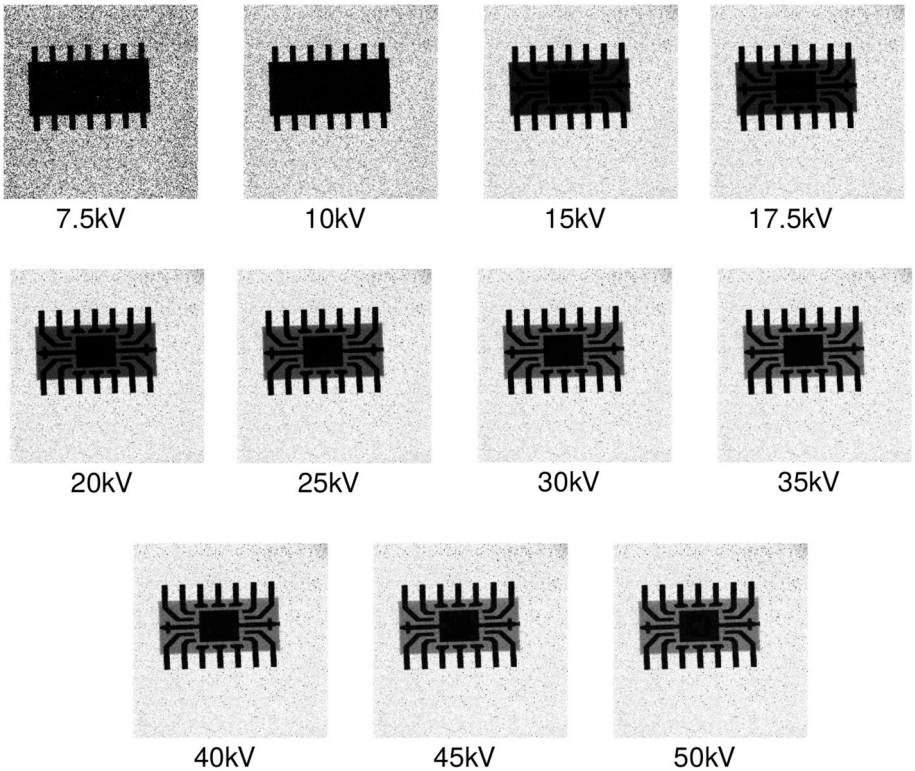

Fig. 3. Radiographic images at different using different X-ray tube voltages using the Timepix detector. The Grayscale is normalized to have the same average brightness outside the chip.

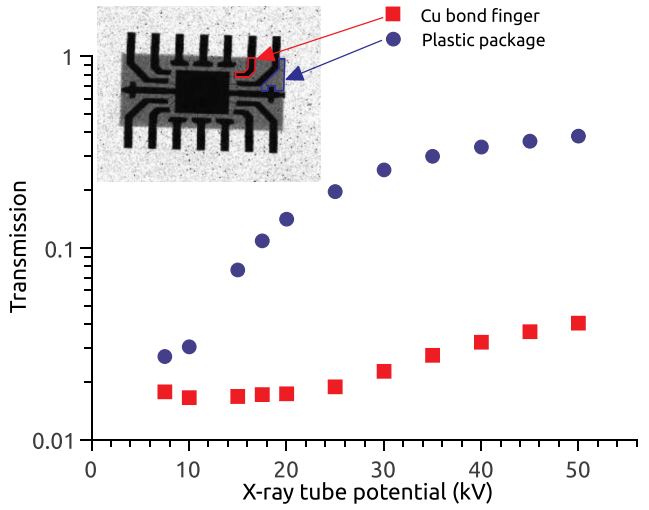

Fig. 4. Transmission of different parts of the chip package as a function of the X-ray tube potential using the Timepix detector. The inset shows the regions shown, the Cu bond finger and the remaining plastic region.

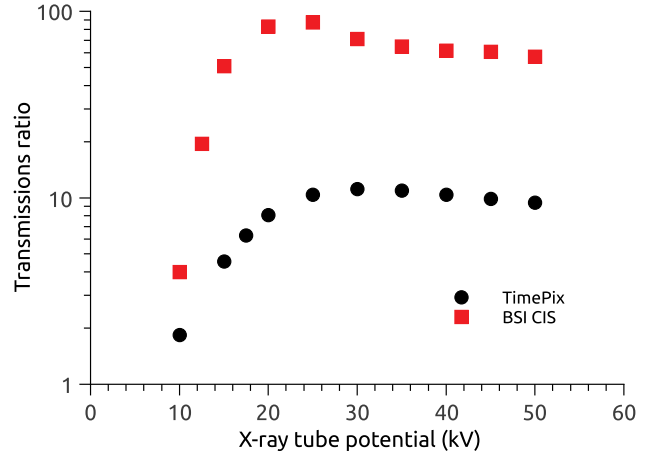

Fig. 5. Ratio of contrasts between plastic package and bonding finger as a function of TBV for the BSI CIS and Timepix.

having more photons—and signal—detected in the regions where the sample strongly attenuates the beam, e.g. in the central pad of the chip. However, if the number of photons detected is sufficiently high to allow the identification of regions with low contrast variations (Alcalde Bessia et al., 2018), the high voltage irradiation can be used to detect features in these darkened regions.

3.3. Construction of false color images varying TBV

Reference (Procz et al., 2009) implements the construction of false color Red-Green-Blue (RGB) images fusioning information obtained at different photon energies. In that work the different spectum is separated using by the Medipix thresholds. In the present work, we propose the use of the three channels to provide complementary information in a similar fashion. We use the red and green channels to show information obtained at 10 kV and 25 kV, which have very different absoption ratios in the different regions of the chip. The blue channel will provide information obtained at 50 kV from the most opaque regions of the sample, increasing 20 times the brightness of the image. This increase in the brightness of one channel will make it saturate in most regions, but will allow to observe radiation opaque regions with more detail, extending the dynamic range visible in the picture.

Fig. 6 shows the construction of an RGB image which fussions the

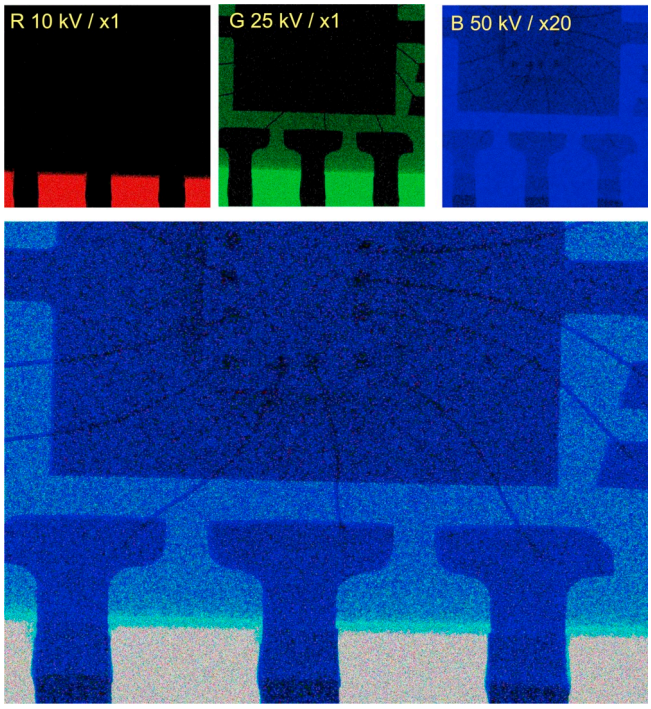

Fig. 6. Fussion of images obtained at different TBV. The red channel is formed by the image obtained at 10 kV, the green channel at 25 kV and the blue channel at 50 kV but with an increase in brightness of 20 times, to give more detail on the regions of low constrast. The fussioned image allows to see simultaneously the bonding fingers, bonding wires, the folded section of the pins, and the contour of the silicon die surrounded by the epoxy used to stick it on the package. (For interpretation of the references to color in this figure legend, the reader is referred to the Web version of this article.)

images obtained at 10 kV, 25 kV and 50 kV. The subplots present the three colored images merged in the main plot, where in a single image visual information from different intensity ranges and materials is presented. The plastic package is observed in cyan, and the bonding pad, fingers and pins are observed in blue. Inside the central pad, the contour of the silicon die of the chip can be observed thanks to the attenuation of the X-rays on the conductive epoxy used to stick the die on the package. The bonding wires are clearly visible, and the blue channel with increased brightness allows the observation of the bonding wires over the central bonding pad, and with some detail the bonding balls, and the borders of the silicon die. The same images obtained with the Timepix detector are shown in Fig. 7.

4. Detection efficiency of the BSI CIS

The measurements of Figs. 2 and 3 required very different times to obtain high number of events, few minutes for the CIS and 10 s using the Timepix. This difference implies applying higher doses to the sample when the CIS is used instead the Timepix due to the lower detection efficiency of the CIS.

To partially quantify this detection efficiency and provide more information about the response of the sensor at higher energies for example for gamma rays dosimetry, several experiments were carried out, obtaining the efficiency from 15.7 keV to 1.33 MeV.

The lower energy photons were obtained by fluorescence exposing high purity metal samples to X-rays from a Moxtek source with a Ag anode. The target materials used were Zr, Pd, and Ag which provide fluorescence spectra with k_α lines in 15.7 keV, 21.2 keV, and 22.1 keV respectively. The CIS was placed at a distance of 11.00.5 cm from the target, and an Amptek X-123 Si Drift Detector (SDD) was placed at 10.00.5 cm from the target to measure the fluorescence photon flux.

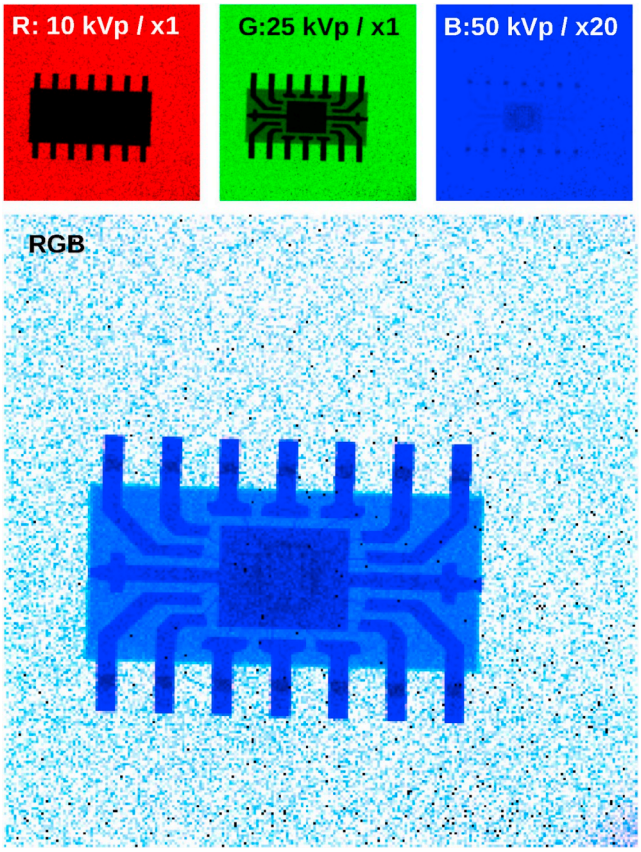

Fig. 7. Fussion of images obtained at different TBV. The red channel is formed by the image obtained at 10 kV, the green channel at 25 kV and the blue channel at 50 kV but with an increase in brightness of 20 times, to give more detail on the regions of low constrast. The fussioned image allows to see simultaneously the bonding fingers, bonding wires, the folded section of the pins, and the contour of the silicon die surrounded by the epoxy used to stick it on the package. (For interpretation of the references to color in this figure legend, the reader is referred to the Web version of this article.)

The SDD has an area of 25 mm^2 and a thickness of 500 μm, and is protected from light by a thin Amptek C1 window (AmptekC and. X-123˚). The number of counts by the SDD was corrected by the transmission of the window and the 500 μm Si detector efficiency (AmptekC and. X-123˚). During each measurement, the SDD and spectrometer were used to verify that the expected spectrum was the expected.

The higher energy photons were obtained using Eckert & Zielgler sealed radioactive sources of ^{109}Cd, ^{133} Ba, ^{137} Cs, ^{60} 60Co, and ^{22} Na. The major emission lines are of 22 keV and 25 keV, 81 keV and 356 keV, 662 keV, 1.17 MeV and 1.33 MeV, and 1.27 MeV respectively (Eidelman et al., 2004). The sources were placed at a distance of 152 mm from the CIS. The flux at the CIS was estimated from the original calibrated activity of the sources corrected by the decay time, and the distance to the CIS.

Each irradiation consisted on exposing the detector during several minutes to obtain a set of images. The images were processed offline identifying the photon interactions as a cluster of pixels with values over a threshold sufficiently high to ensure having a negligible number of false positives, with the algoritm presented by (Alcalde Bessia et al., 2016). In all cases the number of events counted was higher than 2200.

The flux at the CIS was estimated with the counts measured by the SDD, distances and areas. In the range of energies used in the experiment, the absorption of photons in the 25 μm Al layer interposed between the sources and the chip is negligible. Fig. 8 shows the measured quantum efficiency, i.e. the fraction of photons detected by the CIS compared to the flux of photons multiplied by its area. The efficiency is

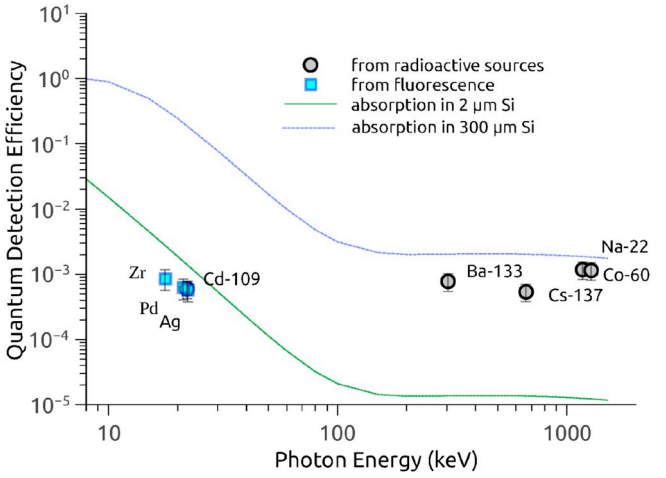

Fig. 8. Quantum efficiency measured on the CIS as a function of photon energy using sealed radioactive sources and X-ray fluorescence from different materials. In cases where the fluorescence or emission have more than one line, the horizontal axis is referred to the most intense line.

in the range from 0.05% to 0.3% in the whole energy range. In the figure, it is also plotted the probability of absorption of photons in 2 μm and 300 μm Si layers. An interesting feature is that the efficiency measured by fluorescence and from radioactive sources at 22 keV overlap within the measurement error showing consistency among the measurements. As was previously mentioned, although the range of energies is wider than the range used for X-ray images in the previous section, the presented efficiency at high energies would be interesting for example for its use in a gamma rays detector.

The BSI CIS efficiency measured in the range from 15.7 keV to 22.5 keV is close but few times lower than the absorption in the Si Layer, probably due to non-negligible probability of rejecting events with signals lower than the acceptance threshold (Perez et al., 2016). On the other hand, the detection efficiency is higher than the absorption in the thin Si layer for the points over 300 keV. This is because at these high energies many photons interact by Compton effect, generating Compton long-range backscaterd electrons below the active region of the BSI CIS. In this case, the CIS can be detecting electrons generated below the active volume after photon absorption in a similar way that the entrance surface dose during gamma rays irradiation is not negligible (Butson et al., 1996).

5. Discussion

This section will discuss differences between the images obtained with both sensors, in first place the spatial resolution, and in second place how the different efficiencies of the sensors affect the contrast observed in the images.

5.1. Spatial resolution and active area

The main advantage and motivation to use the BSI CIS of this work compared to other hybrid pixelated detectors is the much smaller pixel pich, which allows a much higher spatial resolution. As an example Fig. 9 shows in detail a region of the radiographed with the detail of a bonding wire. The image obtained with the CIS does not only allow a clear observation of the region, it also allows an accurate measurement of the bonding wire diameter of 15 μm. The same image obtained with the Timepix does not allow to even notice the wire. On the other hand, the attenuation of the X-rays can be estimated though the intensity of the image, yielding $\simeq$ 30% of attenuation of the 15 μm diameter wire consistent with the fact that these wires are usually composed by Au—taking in account that most of the image is obtained with the

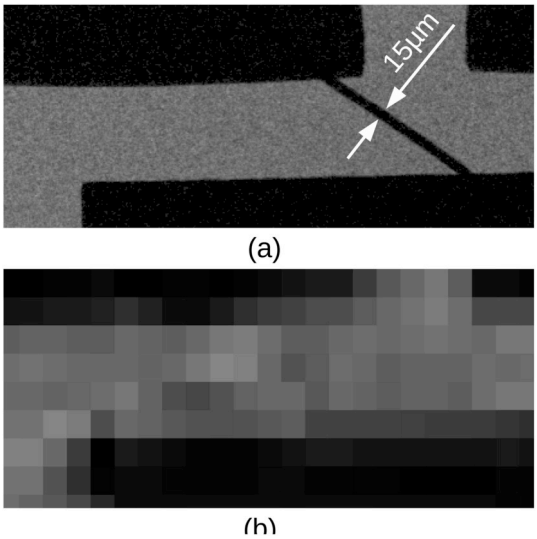

Fig. 9. Image of a region with a bonding wire in obtained with the BSI CIS (a) and with the Timepix (b). The high spatial resolution of the CIS allows a direct measurement of the wire diameter which is not even visible with the Timepix. Both images were obtained at TBV = 50 kV.

higher-end region of the X-ray spectrum not attenuated by the package.

A disadvantage of the CIS BSI compared to the MediPix detector is the smaller active area, problem which can be overcomed taking several images after moving the object with a stepper to then, reconstruct the larger area picture.

5.2. Detection efficiency

The BSI CIS used in this work presents a much lower detection efficiency than its hybrid detector counterpart, detection that can be even three orders of magnitude lower at some energies using the measurement conditions of this work. The main reason for this lower detection efficiency of the CIS at low energies compared to the Medipix is the lower photon absorption probability in the active thickness presented in the continuous lines of Fig. 8. At higher energies, the interaction of photons with the material surrounding the active area of the sensor might explain the high detection efficiency of the BSI CIS despite its small thickness.

The different dependence of the response with energy of the CIS would explain the different contrast ratios observed in Fig. 5.

Also, since each pixel has a smaller area, to have the same number of photons per pixel and thus reach the same shot noise for each pixel, it is necessary to have more photons per unit area, which implies a higher irradiation dose to the sample. This fact, in addition to the lower detection efficiency of the sensor, implies much higher doses to obtain high spatial resolution images, making impossible their use as direct detectors in diagnostic imaging in medicine.

6. Conclusions

This work deals with the use of a BSI CIS to obtain X-ray images, empoying different tube potentials to provide increments in the spectral wide of the beam. A plastic packaged integrated circuit was used as an example of object to analyze. As the energy increases, different contrasts were measured in various regions. The high penetration of photons at highest energies allowed the observation of hidden features of the sample in opaque regions, for example the bonding wires and balls, contour of the silicon die. The whole information could be fussioned in false color images to provide visual information about the whole chip in a single picture. The detection efficiency of the BSI CIS was measured in a wide range of energies, and is in the range of 0.05%–0.3%, lower than the hybrid detector which implies higher irradiation doses to obtain an image.

Acknowledgments

This work was supported by the ICTP Associate program, the ANPCyT under Project PICT 2014–1966 and Project PICT-2015-1644, by UNCuyo under Grant C018, and in part by CONICET under Project PIP 2011-0552 and Project PIP 2013-0077.

Appendix A. Supplementary data

Supplementary data to this article can be found online at https://doi.org/10.1016/j.radphyschem.2019.03.048.

References

Alcalde Bessia, F., Perez, M., Lipovetzky, J., Piunno, N.A., Mateos, H., Sidelnik, I., Blostein, J.J., Sofo Haro, M., Gomez Berisso, M., 2018. X-ray micrographic imaging system based on COTS CMOS sensors. Int. J. Circuit Theory Appl. 46 (10), 1848–1857. URL: https://onlinelibrary.wiley.com/doi/abs/10.1002/cta.2502 10.1002/cta.2502.

Alcalde Bessia, F., Perez, M., Sidelnik, I., Sofo Haro, M., Blostein, J.J., Gomez Berisso, M., Marin, J., Lipovetzky, J., 2016. COTS CMOS active pixel sensors damage after alpha, thermal neutron, and gamma irradiation. In: Argent. Conf. Of Micro-Nanoelecton., Technology. and Applic. (CAMTA). IEEE, pp. 22–26. URL: https://doi.org/10.1109/CAMTA.2016.7574085.

Amptek INC, . X-123SDD Complete X-Ray Spectrometer with Silicon Drift Detector (SDD). URL: http://amptek.com/products/x-123sdd-complete-x-ray-spectrometer-with-silicon-drift-detector-sdd/#5.

Ballabriga, R., Alozy, J., Campbell, M., Frojdh, E., Heijne, E., Koenig, T., Llopart, X., Marchal, J., Pennicard, D., Poikela, T., et al., 2016. Review of hybrid pixel detector readout asics for spectroscopic x-ray imaging. J. Instrum. 11 (01), P01007. URL: https://doi.org/10.1088/1748-0221/11/01/P01007.

Butson, M.J., Rozenfeld, A., Mathur, J.N., Carolan, M., Wong, T.P., Metcalfe, P.E., 1996. A new radiotherapy surface dose detector: the MOSFET. Med. Phys. 23 (5), 655–658. URL: https://doi.org/10.1118/1.597702.

Conti, E., Placidi, P., Biasini, M., Bissi, L., Calandra, A., Checcucci, B., Chiocchini, S., Cicioni, R., Di Lorenzo, R., Dipilato, A.C., et al., 2013. Use of a CMOS image sensor for an active personal dosimeter in interventional radiology. IEEE Trans. Instrum. Meas. 62 (5), 1065–1072. URL: https://doi.org/10.1109/TIM.2012.2223331.

Dmitruk, K., Denkowski, M., Mazur, M., Mikołajczak, P., 2017. Sharpening filter for false color imaging of dual-energy x-ray scans. Signal Image Video Processing 11 (4), 613–620. URL: https://doi.org/10.1007/s11760-016-1001-7.

Eidelman, S., Hayes, K., Olive, K.e., Aguilar-Benitez, M., Amsler, C., Asner, D., Babu, K., Barnett, R., Beringer, J., Burchat, P., et al., 2004. Review of particle physics. Phys. Lett. B 592 (1–4), 1–5.

Holden, W.M., Hoidn, O.R., Ditter, A.S., Seidler, G.T., Kas, J., Stein, J.L., Cossairt, B.M., Kozimor, S.A., Guo, J., Ye, Y., et al., 2017. A compact dispersive refocusing rowland circle X-ray emission spectrometer for laboratory, synchrotron, and XFEL applications. Rev. Sci. Instrum. 88 (7) 073904. URL: https://doi.org/10.1063/1.4994739.

Holden, W.M., Hoidn, O.R., Seidler, G.T., DiChiara, A.D., 2018. A color x-ray camera for 2–6 keV using a mass produced back illuminated complementary metal oxide semiconductor sensor. Rev. Sci. Instrum. 89 (9) 093111. URL: https://doi.org/10.1063/1.5047934.

Imatek, X., 2012. Xri-uno/cdte Manual. Barcelona Spain, Eureka.

Jakuubek, J., 2009. Semiconductor pixel detectors and their applications in life sciences. J. Instrum. 4 (03), P03013. URL: https://doi.org/10.1088/1748-0221/4/03/P03013.

Jambi, L.K., Lees, J.E., Bugby, S., Tipper, S., Alqahtani, M., Perkins, A., 2015. Evaluation of XRI-UNO CdTe detector for nuclear medical imaging. J. Instrum. 10 (06), P06012. URL: https://doi.org/10.1088/1748-0221/10/06/P06012.

Llopart, X., Ballabriga, R., Campbell, M., Tlustos, L., Wong, W., 2007. Timepix, a 65k programmable pixel readout chip for arrival time, energy and/or photon counting measurements. Nucl. Instrum. Methods A 581 (1–2), 485–494. URL: https://doi.org/10.1016/j.nima.2007.08.079.

Paolucci, M., Battisti, D., Biasini, M., Checcucci, B., Di Lorenzo, R., Esposito, A., Fanò, L., Passeri, D., Placidi, P., Servoli, L., 2011. A real time active pixel dosimeter for interventional radiology. Radiat. Meas. 46 (11), 1271–1276. URL: https://doi.org/10.1016/j.radmeas.2011.07.006.

Pérez, M., Blostein, J.J., Alcalde Bessia, F., Tartaglione, A., Sidelnik, I., Haro, M.S., Suárez, S., Gimenez, M.L., Berisso, M.G., Lipovetzky, J., 2018. Thermal neutron detector based on COTS CMOS imagers and a conversion layer containing gadolinium. Nucl. Instrum. Methods A 893, 157–163. URL: https://doi.org/10.1016/j.nima.2018.03.032.

Perez, M., Lipovetzky, J., Haro, M.S., Sidelnik, I., Blostein, J.J., Alcalde Bessia, F., Gomez Berisso, M., 2016. Particle detection and classification using commercial off the shelf CMOS image sensors. Nucl. Instrum. Methods A 827, 171–180. URL: https://doi.org/10.1016/j.nima.2016.04.072.

Procz, S., Lübke, J., Zwerger, A., Fauler, A., Pichotka, M., Mix, M., Fiederle, M., 2010.

Energy selective x-ray imaging with medipix. In: Nucl. Sci. Symposium Conf. Rec. (NSS/MIC), 2010 IEEE. IEEE, pp. 3846–3851. URL: https://doi.org/10.1109/NSSMIC.2010.5874533.

Procz, S., Lubke, J., Zwerger, A., Mix, M., Fiederle, M., 2009. Optimization of medipix-2 threshold masks for spectroscopic x-ray imaging. IEEE Trans. Nucl. Sci. 56 (4), 1795–1799. URL: https://doi.org/10.1109/TNS.2009.2025175.pagina_picam.

RaspberryFoundation. Camera Module. URL: https://www.raspberrypi.org/documentation/hardware/camera/.

Raspberry Pi development group, 2018. Raspberry Model B. Raspberrypi Org Saatavissa. 2018. https://www_raspberrypiorg/products/raspberry-pi-3-model-b/Hakupaiva6.

Schlomka, J., Roessl, E., Dorscheid, R., Dill, S., Martens, G., Istel, T., Bäumer, C., Herrmann, C., Steadman, R., Zeitler, G., et al., 2008. Experimental feasibility of multi-energy photon-counting K-edge imaging in pre-clinical computed tomography. Phys. Med. Biol. 53 (15), 4031. URL: https://doi.org/10.1088/0031-9155/53/15/002.

Zhang, G., Dai, T., Yang, H.. 2009. Backside illuminated image sensor with global shutter and storage capacitor. US Pat. App. 12/028,659.

Zhao, W., Sakurai, K., 2017. Seeing elements by visible-light digital camera. Sci. Rep. 7, 45472. URL: https://doi.org/10.1038/srep45472.

Zhao, W., Sakurai, K., 2019. Multi-element X-ray movie imaging with a visible-light CMOS camera. J. Synchrotron Radiat. 26 (1), 230–233. https://doi.org/10.1107/S1600577518014273. URL: https://doi.org/10.1107/S1600577518014273.